1 ### *In Situ* Techniques for Aqueous Quinone-Mediated Electrochemical Carbon Capture and Release

2 Kiana Amini[1,3], Thomas Cochard[1], Yan Jing[2,4], Jordan D. Sosa[1], Dawei Xi[1], Maia Alberts[1], Michael S.
3 Emanuel[1], Emily F. Kerr[2], Roy G. Gordon[2], Michael J. Aziz[1✉]

4 [1.] John A. Paulson School of Engineering and Applied Sciences, Harvard University, Cambridge, Massachusetts 02138,
5 United States
6 [2.] Department of Chemistry and Chemical Biology, Harvard University, Cambridge, Massachusetts 02138, United States
7 [3.] Present address: Department of Materials Engineering, The University of British Columbia, Vancouver, BC Canada V6T
8 1Z4
9 [4.] Present address: Department of Materials Science and Engineering, National University of Singapore, 117575, Singapore

10 ✉ E-mail: maziz@harvard.edu

Abstract

12 In this work, we elucidate the intricate interplay between the nucleophilicity-swing and pH-swing
13 mechanisms in aqueous quinone-mediated carbon capture systems, showcasing the critical role of
14 understanding this interplay in the material discovery cycle. This insight prompts the development of two
15 *in situ* techniques. The first technique employs *in situ* reference electrodes and capitalizes on discernible
16 voltage signature differences between quinones and quinone-CO_2 adducts, allowing for the quantification
17 of the isolated contributions of the two mechanisms. The second method is developed based on our finding
18 that the adduct form of the quinone exhibits a fluorescence emission from an incident light at wavelengths
19 distinct from the fluorescence of the reduced form. Thus, we introduce a non-invasive, *in situ* approach
20 using fluorescence microscopy, providing the capability to distinguish species with sub-second time
21 resolution at single-digit micrometer resolution. This technique holds promise for studying quinone-based
22 systems for carbon capture and beyond.

Introduction

24 Effective carbon management is vital for addressing emissions from some of the toughest-to-abate sectors,
25 such as heavy industries like steel production and cement manufacturing [1]. The conventional approach
26 to capturing CO_2 from dilute sources involves amine scrubbing technology, where CO_2 is captured at 40°C
27 and released at 120°C [2, 3]. [3]. In pursuit of more efficient alternatives, researchers have directed their
28 focus toward the development of electrochemical technologies for this purpose. Electrochemical systems
29 offer the advantage of isothermal operation, relying on an electrical gradient to drive a redox reaction that
30 can directly or indirectly create an affinity in the system for CO_2 capture [4-10].

31 One of the promising electrochemical carbon capture systems relies on quinone chemistry. Quinones
32 exhibit two potential mechanisms of CO_2 capture. Firstly, the nucleophilicity-swing mechanism occurs,
33 where the phenolate groups upon quinone reduction reversibly react with carbon dioxide via nucleophilic
34 addition, which results in the formation of quinone-CO_2 adducts. This mechanism is observed with
35 quinones dissolved in aprotic solvents [11-13] or immobilized on the electrodes [7,11,14,15]. However, in
36 protic solvents, depending on the pK_a of the hydroquinones and the local pH, the electrochemical reduction
37 of quinones can be proton-coupled and create hydroxide ions, which capture CO_2 as carbonate or
38 bicarbonate [16-18]. Thus, in an aqueous solvent, both pH-swing and nucleophilicity-swing mechanisms
39 may contribute to CO_2 capture across a range of operational conditions. However, traditional methods of
40 measuring the total amount of CO_2 captured or released allow for reporting only the combined contribution
41 of these two mechanisms; the relative contributions are unknown. We expect continued progress in
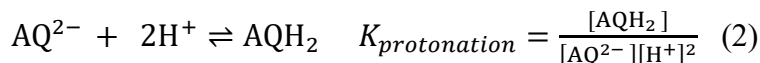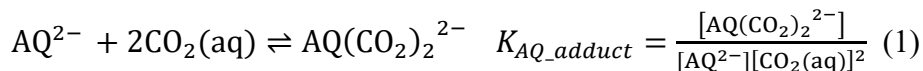
developing aqueous quinone-based technologies for carbon capture, attracted by the safety, economic viability, and excellent ionic conductivity offered by water serving as a solvent. However, to pave the way for these innovations, it is essential to deepen our understanding of the underlying mechanisms and their relative contributions to overall process performance.

In this study, we address the need to quantify the contributions of the nucleophilicity-swing and pH-swing mechanisms. The first two sections lay the foundation for this exploration. Firstly, we provide a thermodynamic overview elucidating the interplay between these mechanisms, emphasizing how the dominance of one over the other influences critical performance metrics of the final engineered electrochemical cell and necessitates specific molecular engineering considerations in the context of the material discovery cycle. Secondly, we delve into a case study focusing on bis[3-(trimethylammonio)propyl]-anthraquinones (BTMAPAQs) [16], extracting both thermodynamic and kinetic insights for its three isomers. Building on these foundational sections, we introduce two *in situ* experimental methods for quantifying the contributions of these mechanisms in the system.
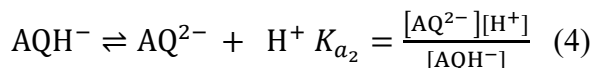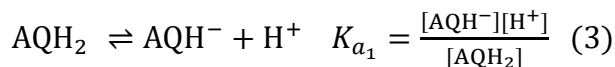
Results and Discussion

Thermodynamic Overview

To demonstrate the influence of various properties of the hypothetical anthraquinone molecule employed in the system on the interplay between nucleophilicity-swing and pH-swing mechanisms, we analyze a set of reaction equilibrium equations inherent to the system. The fully reduced anthraquinone (AQ^{2-}) molecule in an aqueous solution can either undergo the direct capture of CO_2 through $AQ(CO_2)_2^{2-}$ adduct formation or engage in a proton-coupled reaction:

$$AQ^{2-} + 2CO_2(aq) \rightleftharpoons AQ(CO_2)_2^{2-} \quad K_{AQ\_adduct} = \frac{[AQ(CO_2)_2^{2-}]}{[AQ^{2-}][CO_2(aq)]^2} \quad (1)$$

$$AQ^{2-} + 2H^+ \rightleftharpoons AQH_2 \quad K_{protonation} = \frac{[AQH_2]}{[AQ^{2-}][H^+]^2} \quad (2)$$

where the K_{AQ_adduct} and $K_{protonation}$ are the $AQ(CO_2)_2^{2-}$ adduct formation and protonation equilibrium constants, respectively. Both reactions can occur in two steps, involving the sequential acceptance of the first CO_2 or H^+ molecule followed by the second. The experimental determination of K_{AQ_adduct} is elucidated in the next section through cyclic voltammetry, although extracting the equilibrium constant for the initial step in isolation presents challenges. Conversely, the double step protonation/deprotonation can be deduced from the Pourbaix diagram, resulting in the following equilibrium equations:

$$AQH_2 \rightleftharpoons AQH^- + H^+ \quad K_{a_1} = \frac{[AQH^-][H^+]}{[AQH_2]} \quad (3)$$

$$AQH^- \rightleftharpoons AQ^{2-} + H^+ \quad K_{a_2} = \frac{[AQ^{2-}][H^+]}{[AQH^-]} \quad (4)$$

In these reactions, K_{a_1} and K_{a_2} are the equilibrium constants for the first and second deprotonation steps, respectively. The corresponding pK_a values are calculated by taking the negative base-10 logarithm of K_a. For reactions 3 and 4, occurring from right to left (protonation reaction), the result is the consumption of protons and an increase in the pH of the solution. The produced hydroxides can then undergo bicarbonate and carbonate formation reactions, resulting in an indirect capture of CO_2:

$$80 \qquad CO_2(aq) + H_2O \rightleftharpoons HCO_3^- + H^+ \quad K_4 = \frac{[HCO_3^-][H^+]}{[CO_2(aq)]} \quad (5)$$

$$81 \qquad HCO_3^- \rightleftharpoons CO_3^{2-} + H^+ \quad K_5 = \frac{[CO_3^{2-}][H^+]}{[HCO_3^-]} \quad (6)$$

82 Reactions (1) – (6) involve the consumption or production of various charge species. In the solution, charge
83 neutrality must always be maintained. Thus,

$$84 \qquad + 2[AQ^{2-}] + 2[AQ(CO_2)_2^{2-}] + [AQH^-] + [OH^-] + [HCO_3^-] + 2[CO_3^{2-}] - [H^+] - [M^+] = 0 \quad (7)$$

85 where M^+ represents the counterion resulting from dissolving the anthraquinone salt in the solution (for
86 example, K^+or Na^+). Additionally, the sum of concentrations of all AQ-containing molecules is conserved
87 at its total dissolved concentration (C_T). Therefore,

$$88 \qquad + [AQ^{2-}] + [AQ(CO_2)_2^{2-}] + [AQH^-] + [AQH_2] - (C_T) = 0 \quad (8)$$

89 An additional constraint arises from the water dissociation equilibrium resulting in:

$$90 \qquad H_2O \rightleftharpoons OH^- + H^+ \quad K_w = [OH^-][H^+] \quad (9)$$

91 Finally, the concentration of the $CO_2(aq)$ is dictated by the partial pressure of CO_2 (pCO_2) and follows
92 Henry's Law:

$$93 \qquad [CO_2(aq)] = C_{Henry}pCO_2 \quad (10)$$

94 where C_{Henry} is the Henry's constant, taken to be 35 mM/bar at room temperature [9], representing its
95 solubility in water and assumed to be unchanged in the presence of 0.1 M AQ. Given that the present
96 thermodynamic analysis serves as an overview of the interplay between the nucleophilicity-swing and pH-
97 swing mechanisms, we focus on the above main reactions while those leading to intermediate compounds
98 such as $AQ(CO_2)^{2-}$ and $AQHCO_2^-$ and species formed due to mixed mechanisms are assumed to be
99 disregarded for lack of estimation for them and for simplicity.

100 Here, we begin by considering a total concentration of 0.1 M AQ dissolved under a partial pressure of 0.1
101 bar. With pK_{a1} and pK_{a2} set at 11 and 13, respectively—values typical for several anthrahydroquinones
102 reported to date [16,19-21]—we further consider equilibrium constants K_4, K_5, and K_w as $1.1 * 10^{-6}$ M
103 [22], $4.1 * 10^{-10}$ M [22], and 10^{-14} M^2, respectively. Regarding the equilibrium constants for
104 bicarbonate and carbonate formation, we assume that the presence of 0.1 M AQ has not significantly
105 altered the salinity of the solution and the numbers are taken at salinity of zero. Under these specified
106 conditions, Figure 1a illustrates the dynamic interplay between nucleophilicity-swing and pH-swing
107 mechanisms in the capture of CO_2, as a function of the $AQ(CO_2)_2^{2-}$ adduct formation equilibrium
108 constant. This analysis predicts that at K_{AQ_adduct} less than 10^{12} M^{-2}, the thermodynamic driving force
109 for nucleophilicity-swing mechanism is too low and thus the CO_2 capture proceeds mainly via pH-swing
110 mechanism. The opposite is correct for K_{AQ_adduct} values above 10^{17} M^{-2}. Between these two limits, both
111 mechanisms contribute to the capture of CO_2. Understanding this interplay in relation to the properties of
112 the employed molecule is crucial in the context of the material discovery cycle for carbon capture
113 applications. For instance, if a newly synthesized molecule, under the desired operational conditions,
114 exhibits primarily the pH-swing capture mechanism, optimizing the molecule's capture capacity
115 necessitates a focus on maximizing its pK_a, as well as solubility, to increase the concentration of OH⁻

molecules produced. Conversely, for molecules with strong adduct formation equilibrium constants, maximizing pK_a becomes irrelevant, and attention should be directed merely toward enhancing the solubility of the AQ molecule. It is important to note that basicity and nucleophilicity are intrinsically linked, as both properties are governed by the electron-donating ability of the molecule. Consequently, these properties cannot be independently modified in isolation. However, molecular structure can be strategically optimized to favor either of the two mechanisms (examples are provided in SI Section 3). Results of such optimization are illustrated in Figures 1b-c and S1. For intermediate values of K_{AQ_adduct} (for example, 10^{14} M^{-2}), where both mechanisms are at play, increasing the pK_a of the AQ molecule shifts the contribution more toward bicarbonate/carbonate formation, as depicted in Figure 1b and the zoomed-in image in Figure S1d. In contrast, under conditions where K_{AQ_adduct} is strong (for example, 10^{22} M^{-2}), even with limited pK_a values (for example, $pK_{a1} = 7$ and $pK_{a2} = 7$), the AQ$(CO_2)_2^{2-}$ adduct formation mechanism captures up to the expected capacity independent of enhancements in pK_{a2} (see Figure S1a). However, under such limiting conditions, when K_{AQ_adduct} is weak (for example, 10^4 M^{-2}), increasing the pK_a of anthrahydroquinone molecule becomes a crucial factor for enhancing the capture capacity as depicted in Figure S1a. Note that capture capacity is defined as the molar ratio of CO₂ molecules captured to AQ molecules present.

Another important factor is the effect of CO₂ partial pressure. Under the conditions set in Figure 1a and for intermediate values of K_{AQ_adduct} (for example, 10^{14} M^{-2}), where both mechanisms are at play, increasing pCO_2 to values higher than 0.1 bar, would indeed increase the $CO_2(aq)$ concentration according to the Henry's law, but it results in negligible change in the individual contribution of nucleophilicity-swing and pH-swing mechanisms toward the total capture, as shown in Figure 1c and Figure 1d. However, at dilute CO₂ concentrations (less than 0.05 bar), the thermodynamic driving force for AQ$(CO_2)_2^{2-}$ adduct formation drops and in the bicarbonate/carbonate equilibration, carbonate formation contribution increases, which would have effect on the capacity of the capture. In the adduct formation pathway, each AQ molecule captures two CO₂ molecules by engaging both nucleophilic oxygen sites. Meanwhile, in the pH-swing pathway, a two-step protonation process yields two OH⁻ ions per AQ molecule. When these hydroxides predominantly form bicarbonate groups, each OH⁻ captures one CO₂, resulting in a 2 CO₂ capture capacity per one AQ molecule. Contrastingly, carbonate formation consumes two OH⁻ ions, resulting in a 1 CO₂ capture capacity per one AQ molecule. Therefore, AQ$(CO_2)_2^{2-}$ adduct formation and bicarbonate formation both exhibit a capture capacity ratio of 2 to 1, while carbonate formation yields a 1 to 1 ratio. In the context of the interplay between nucleophilicity-swing and pH-swing mechanisms, one can see that for the molecules where K_{AQ_adduct} is strong (for example, 10^{22} M^{-2}), the thermodynamic driving force for AQ$(CO_2)_2^{2-}$ adduct formation is very strong, and even at dilute CO₂ concentrations (400 ppm), the capture capacity proceeds at a 2-1 ratio through nucleophilicity-swing mechanisms (see Figure S1b). Conversely, when K_{AQ_adduct} is weak (for example, 10^4 M^{-2}), the dominant mechanism becomes pH-swing, and reducing pCO_2 to values less than 0.05 bar shifts the equilibrium toward carbonate formation, diminishing the capture capacity to a 1 to 1 ratio, which is particularly relevant for cells engineered for direct air capture (DAC), where CO₂ partial pressure is low. The potential impact of these mechanisms on the performance is further discussed in the SI Section 2. -

Thermodynamic and Kinetic Analysis of BTMAPAQ Isomers

In this section, we present a case study for the specific case of BTMAPAQ isomers [16], as a representative compound in aqueous quinone-mediated carbon capture systems. Figures 2a-c illustrate the cyclic voltammetry of 1,4-, 1,5-, and 1,8-BTMAPAQ isomers at various scan rates under a pure stream of CO_2 and at one scan rate under pure N_2. The CV plots of the isomers at all other scan rates under a pure N_2 headspace is further shown in Figure S2 (SI Section 4.1). For each isomer, a new oxidation peak emerges under the CO_2 headspace, shifted to more positive potentials compared to that under pure N_2 headspace, while the reduction peak remains almost identical. The more positive oxidation peak corresponds to the newly formed $AQ(CO_2)_2{}^{2-}$ redox-active species, which cannot exist under the pure nitrogen environment. The less positive redox potential is attributed to the AQ^{2-} oxidation given that it is occurring under the nitrogen headspace. In the nucleophilicity-swing mechanism, the oxidation potential of $AQ(CO_2)_2{}^{2-}$ is significantly more positive compared to the pH-swing mechanism, where AQH_2 demonstrates a more negative oxidation peak, proximal to the reduction peaks of AQ^{2-}. These differences critically influence the thermodynamic energy requirements and oxygen stability of the system (SI Section 2). In the thermodynamic context, the equilibrium constants for $AQ(CO_2)_2{}^{2-}$ adduct formation (K_{AQ_adduct}) for these isomers can be deduced by examining the difference in the half-wave potential peaks associated with the AQ^{2-} and $AQ(CO_2)_2{}^{2-}$ redox reactions [23] through Equation S1 (derivation included in SI Section 4.2). Using Equation S1, we find the K_{AQ_adduct} to be $1.6 * 10^{22}$, $7.3 * 10^{21}$ and $2.8 * 10^{18}$ M^{-2} for the isomers 1,4-, 1-5, and 1-8-BTMAPAQ, respectively. Comparing with the predictions from the equilibrium model shown in Figure 1a, these are attributed to a very strong $AQ(CO_2)_2{}^{2-}$ adduct formation region, predicting a system dominated by nucleophilicity-swing mechanism.

In order to gain some understanding of the kinetics of the reaction, we conducted the CV tests under different scan rates as shown in Figures 2a-c. At higher scan rates, the CV is swept faster across the same potential range, resulting in a quicker run. Given that under CO_2, a chemical reaction is occurring $(AQ(CO_2)_2{}^{2-}$ adduct formation, according to reaction (1)), there would be less time for the chemical reaction to proceed at higher scan rates. It can be observed that for the 1,4- and 1,5-BTMAPAQ isomers, increasing the scan rate would barely result in any current being extracted at the oxidation potential attributed to the oxidation of AQ^{2-}, which implies that the chemical quinone-adduct formation reaction is occurring at rates faster than the scan rates used. Thus, even at 1000 mV/s, we extract current predominantly from $AQ(CO_2)_2{}^{2-}$. Interestingly, for the 1,8-BTMAPAQ isomer, increasing the scan rate reveals a growing peak at the oxidation potentials related to AQ^{2-} oxidation, which indicates that the chemical reaction rate of $AQ(CO_2)_2{}^{2-}$ adduct formation is slower for this isomer compared to the other two isomers and cannot keep up with the fast rate of potential change. In order to quantify the kinetic rates associated with the $AQ(CO_2)_2{}^{2-}$ adduct formation reaction, we fit experimental CV data to a reaction scheme assuming an electrochemical-chemical-electrochemical (ECE) mechanism, with details extensively described in the SI Sections 4.3 - 4.6. Examples of a fitting for 1,8-BTMAPAQ are shown in Figure 2d, and the rest of the fittings are provided in Figures S5-S7, indicating a very good agreement between the model and the experimental data. For 1,4- and 1,5-BTMAPAQ isomers, an increase in scan rate barely results in current extraction at the potential relevant to AQ reduction. Therefore, we report a lower limit on k_c for these two isomers, below which the chemical reaction would be too slow to keep up with the fast scan rates. However, for 1,8-BTMAPAQ, an exact value of k_c, rather than a limit, is reported.

The extracted parameters for the three isomers are presented in Table S1. The k_c values are >6.7, >6.0, 2.4 s^{-1} which would be >192, >171, and 68.6 $M^{-1}s^{-1}$ (per moles of CO_2) for 1,4-, 1,5-, and 1,8-BTMAPAQ

isomers, respectively, indicating the rate constant for the occurrence of the nucleophilicity-swing mechanism. In contrast, the rate constant for bicarbonate/carbonate formation that is occurring in the pH-swing mechanism is reported to be $12.1 * 10^3 \ M^{-1}s^{-1}$ at 25°C [24], significantly higher than what we are reporting for the $BTMAPAQ(CO_2)_2{}^{2-}$ adduct formation mechanism. Having obtained the rate constants, we can predict the rates of both bicarbonate formation and the formation of the $BTMAPAQ(CO_2)_2{}^{2-}$ adduct under various conditions (SI Section 4.7), which demonstrates the extent to which bicarbonate formation can proceed more rapidly than the $BTMAPAQ(CO_2)_2{}^{2-}$ adduct formation. This comparison highlights that although thermodynamically we predict the adduct formation mechanism to occur predominantly for these three isomers, kinetically the pH-swing mechanism is faster. As such, each mechanism exhibits different kinetic and reaction rates, which affect the overall rate of CO_2 capture in the designed system (SI Section 2).

In Situ Methods

The previous two sections underscore the necessity for an experimental methodology capable of discerning the intricate interplay between the pH-swing and nucleophilicity-swing mechanisms. (SI Section 2). As shown in Figure S12, using pH as an indicator for the amount of OH$^-$ formed during the reaction is insufficient, primarily due to the buffering effect of the carbonate/bicarbonate system. In the following sections, we introduce two *in situ* experimental techniques designed for this purpose.

In Situ Method 1: Reference Electrodes

The cyclic voltammetry plots depicted in Figure 2 reveal the distinct oxidation potential signature of the $BTMAPAQ(CO_2)_2{}^{2-}$ adduct in comparison to the reduced BTMAPAQ molecules. This discernible voltage separation, observed in multiple cases of other quinones [7,23], should allow us to accurately quantify the contribution of nucleophilicity-swing toward total carbon capture. To illustrate this method and investigate its sensitivity, we conducted experiments utilizing a flow cell equipped with a reference electrode on the negative side (BTMAPAQ side), which allows us to measure the real-time potential of the negative electrode against the reference electrode (See SI Section 5.1). Utilizing this setup, the cell was intentionally charged (see SI 5.1) in a nitrogen environment, followed by a controlled purge with 0.1 bar CO_2 and 0.9 bar of N_2 for varying durations (60 minutes in Figure 3a), followed by a switch back to the nitrogen environment. This experimental procedure with different CO_2 purge durations (15, 30, and 60 minutes) was intentionally designed to allow us to control the amount of adduct formation during the course of the experiment and examine its relationship with the discharge voltage profiles (See SI Sections 5.2 and 5.3 for flow battery operation details, experimental setup, and calibration procedure).

The voltage profile depicted in Figure 3a is zoomed in the upper plot of Figure 3b, accompanied by its corresponding negative half-cell potential measured from the reference electrode. Two distinct plateaus emerge in the full cell voltage profile (the dashed gray square in Figure 3a), mirroring the double plateaus identified in the negative half-cell potential plot. The more negative discharge potential, averaged at -0.3 V vs SHE, aligns well with the oxidation potential of the reduced species from the cyclic voltammetry profiles, while the less negative half-cell potential at 0.1 V vs SHE is close to the adduct species' potential signature. We attribute the differences between the cell potential and the CV potentials to the possible local pH and electrolyte composition differences (See SI Section 5.5 for an explanation of the variation of half-

cell potentials across experiments.). Given this distinctive potential separation, we can calculate the adduct formation by examining the capacity delivered at the voltage signature of the quinone-adduct compound. As depicted in Figure 3c, extending the duration of purging with CO_2 from 15 minutes to 60 minutes clearly shows an increase in the capacity delivered at the potential signature of the adduct species. In separate experiments, we purged with 0.1 bar CO_2/0.9 bar of N_2 from the beginning of the experiment with a 120-minute purging during the rest-time, clearly demonstrating that such a prolonged purging duration would increase the capacity delivered by the adduct. Eventually, in the case of 7 hours of purging, the entire discharge capacity is exclusively delivered by the $BTMAPAQ(CO_2)_2^{2-}$ adduct species.

Figure 3d (top) illustrates the CO_2 release volume calculated both from sensor measurements and the oxidation voltage signature of the $BTMAPAQ(CO_2)_2^{2-}$ adduct for experiments done in Figure 3a and 3b (see SI Section 5.4). The volume obtained from the sensor includes the combined contribution of nucleophilicity-swing and pH-swing mechanisms (dashed red squares in Figure 3a), while the CO_2 volume determined by deducing the adduct concentration from the half-cell discharge voltages represents solely the contribution of the $BTMAPAQ(CO_2)_2^{2-}$ adduct. As a result, the disparity between these two values is attributed to the pH-swing mechanism. Interestingly, the contribution of the pH-swing mechanism versus the nucleophilicity-swing mechanism changes across these experiments. In Figure 3d (bottom), the percentage contribution of each mechanism to the total capture amount is presented. For the short 15-minute duration tests, we observe a 40% contribution from the pH-swing mechanism. However, with a prolonged 7-hour purge time, the capture predominantly occurs through the nucleophilicity mechanism. This observation aligns very well with our earlier discussions on the thermodynamic and kinetic predictions for the BTMAPAQ isomers, demonstrating slow kinetics of nucleophilicity-swing mechanism compared to the pH-swing mechanism but eventual equilibrium domination of the nucleophilicity-swing mechanism. Given that the short experiments show a 40% contribution from the pH-swing mechanism, but complete dominance of the nucleophilicity-swing mechanism during longer purge times, it indicates that if the molecules were detected in real-time during capture phase, there is expected to be an exchange reaction between the organic carbonate adduct and inorganic carbonate. This observation draws parallels to the reported self-exchange electron-transfer reactions observed between diamagnetic and paramagnetic ions of anthraquinones [25]. The observed potential exchange reaction is intriguing and warrants further investigation. In order to show the applicability of the method, we conducted the method under different sets of conditions, i.e., tests for a different isomer 1,4-BTMAPAQ at high concentrations of 0.4 M and very diluted CO_2 concentrations of 0.01 (1% CO_2, 99% N2) (see Figure S20). At these high AQ concentrations, the salinity of the solution deviates from the assumptions made in our equilibrium modeling scheme, and thus we do not draw expectations from our model. However, we can expect that the high AQ concentration combined with the dilute CO_2 partial pressure should significantly increase the likelihood of AQ binding with CO_2 over bicarbonate/carbonate formation. Figure 3e illustrates the measurements conducted over different durations of purge time (1 – 10 hours). In these experiments at high concentrations of BTMAPAQ, we indeed observe the dominance of the nucleophilicity-swing mechanism in all tests. Note that, owing to the extremely low concentrations of CO_2, extended purge durations are necessary to achieve high capture capacities.

Note that in this electrolyte, effectively a mixture of two redox-active species (reduced and the adduct) has formed. As per our prior work on mixed organic redox-active species [26], when the potential separation between two mixed species is over 300 mV, the concentration of the first redox species is consumed before the second redox event begins. This means that for the present case, the capacity at each plateau can be directly correlated with the corresponding species concentration. However, for close potential separations

284 (<300 mV), a modeling scheme such as the one developed in our prior work [26] must be used for the
285 accurate prediction of the concentrations.

286 It is crucial to note that although this method is conducted *in situ*, meaning measurements are taken during
287 the test, it is essentially an 'aftermath' method, as we cannot quantify the concentration of the quinone-
288 adduct species until the discharge occurs and we examine the discharge voltage profiles. In the next
289 section, we introduce a method for real-time measurement of the adduct during the capture phase.

In Situ Method 2: Fluorescence Microscopy-Based Visualization

291 We first investigate the real-time absorbance of the 1,5-BTMAPAQ species by integrating an *in situ*
292 ultraviolet–visible (UV-Vis) spectrometer into the electrolyte flow path in an operating flow cell, as
293 illustrated in Figure S23. Figure 4a presents the absorbance spectra of 5 mM 1-5,BTMAPAQ in 1 M KCl
294 within a flow cell, operating against 20 mM BTMAPFc under a 100% N_2 stream to capture the real-time
295 absorbance profiles during reduction of 1,5-BTMAPAQ in the absence of any 1,5-BTMAPAQ$(CO_2)_2^{2-}$
296 adduct. Under these conditions, five distinct peaks at wavelengths of 223 nm, 251 nm, and 391 nm, 487
297 nm and 523 nm are evident. During charging, the 223 nm peak decreases in absorbance, and the 251 nm
298 and 391 nm peaks increase, with a new peak emerging at 430 nm, corresponding to the conversion of the
299 molecule from its oxidized form to the reduced form. Subsequently, the battery was brought to rest, and
300 UV-Vis spectra were monitored as a 50% CO_2/50% N_2 stream is introduced to form the adduct (Figure
301 4b). Comparing the spectra at t = 0 and after half an hour of purging with CO_2, we observed minor
302 absorbance changes, particularly at 251 nm, 391 nm and 487 nm, indicating a similarity between the
303 spectra of the reduced species and the adduct, which poses a challenge for precise quantification of the
304 species using this method. Further experiments described in SI Section 6.1 similarly revealed minor
305 changes between the two spectra. Consequently, we shifted our focus to fluorescence spectroscopy.

306 Figures 4c and 4d present the emission spectra of the oxidized, reduced, and adduct species of 1,5-
307 BTMAPAQ, obtained *ex situ* using a fluorescent plate reader (experimental details in SI Section 6.3).
308 Figures 4c and 4d illustrate the emission spectra of species excited at 405 nm and 475 nm, respectively. In
309 both cases, the oxidized species shows almost no fluorescence, whereas interestingly, both the reduced and
310 the adduct species exhibit fluorescence, with the adduct form displaying significantly higher intensity. This
311 intriguing trend doesn't appear to be unique to our molecule. We observed a similarly high fluorescence
312 intensity in the adduct for other anthraquinones, including 2,2′-((9,10-dioxo-9,10-dihydroanthracene-2,6-
313 diyl)bis(oxy))-dipropionic acid (2,6-D2PEAQ [19]) and 2-2-propionate ether anthraquinone (22PEAQ
314 [27]), as demonstrated in Figure S25. Note that the solutions contain mixtures of different forms of the
315 anthraquinone, for example the reduced solution contains the collection of AQ^{2-} as well as AQH^- and
316 AQH_2. This mixture may induce diverse energy transition states, influencing the emission intensity in
317 response to varying excitation wavelengths. However, the noteworthy insight gathered from these figures
318 is that, through a careful selection of emission wavelength regions, we can identify areas where the
319 fluorescence signatures of the reduced, oxidized, and adduct species of 1,5-BTMAPAQ are distinct enough
320 to potentially enable quantification of the BTMAPAQ$(CO_2)_2^{2-}$. Specifically, when considering an emission
321 wavelength close to 520 nm for compounds excited at 405 nm (Figure 4c), we observe that the adduct
322 form still exhibits high fluorescence, while the reduced species approaches the bottom of its emission peak.
323 Conversely, at an emission wavelength near 600 nm for compounds excited at 475 nm (Figure 4d), the
324 opposite is observed Furthermore, the emission spectra of the pure bicarbonate/carbonate solutions do not
325 show any fluorescence properties that differ from the background pH 14 solution, as depicted in Figure
326 S26. This emission analysis procedure can be adapted for different conditions (see SI Section 6.2).

327

Next, we proceeded by developing a custom-designed optically transparent microfluidic electrochemical flow cell (Figure 5a) that can be integrated into a fluorescence microscope and is compatible with optical imaging. Figure 5b displays the widefield image of the porous electrode extracted from this cell, while Figure 5c provides a schematic of the experimental setup (see SI Section 6.4). To investigate the potential correlation between fluorescence intensity at wavelengths identified by the *ex situ* study and the adduct concentration, we designed an experiment wherein the battery is initially charged under N_2, followed by the introduction of CO_2. Figures 5d and 5e present the data associated with the operation of the described microfluidic cell under the fluorescent microscope, where two channels with different excitation/absorption settings were established for monitoring, one with excitation-emission wavelengths of 488 – 594 nm and the other with 405-521 nm, respectively. At the initial time point (t_0=0), no fluorescence is evident, consistent with the *ex situ* data, attributed to the oxidized compound not fluorescing within the chosen wavelengths. As the charging process begins and progresses under a nitrogen atmosphere, the reduced form becomes fluorescent (channel 1, t_1 = 2894.5 s), with intensity increasing alongside the charging capacity. During this period, there is a minor change in the fluorescence intensity of channel 2, as expected due to the absence of any adduct species. Subsequent purging with CO_2 (1 bar) induces the conversion of the reduced form to the CO_2-quinone adduct, resulting in the loss of fluorescence in channel 1. Meanwhile, channel 2, characterized by a distinct fluorescence signal from the adduct, becomes intense. Upon discharging, the fluorescence gradually fades (t_3 = 4140.5). During the discharging phase, we intentionally altered the discharge current rate to demonstrate the correlation between the intensity change and the rate of discharge, as evidenced by the comparison between the discharge capacity and intensity plots in Figure 5d. CO_2 gas bubbles formed as a result of the CO_2 release during discharge are also evident (see Video S1), more clearly observed near the outlet of the cell where bubble accumulation occurs.

While the intensity appears to correlate with the concentration of the $BTMAPAQ(CO_2)_2^{2-}$ adduct, for this method to be applicable for quantification we must calibrate the measurement, i.e. establish a correlation between intensity and concentration under a known condition. The most rigorous approach is either to inject a known concentration of the isolated solution of adduct into the cell and measure the emission intensity or to upgrade the setup with a downstream CO_2 sensor and flow meter and a reference electrode. This allows for measuring the potential of the negative half-cell against a reference under a known condition, creating a standard concentration-intensity calibration plot. In this proof of concept, we make an assumption that operating the microfluidic cell under a pure stream of CO_2 (1 bar) from the beginning of the charging process facilitates $BTMAPAQ(CO_2)_2^{2-}$ adduct formation and results in the full dominance of $BTMAPAQ(CO_2)_2^{2-}$ adduct, consistent with our thermodynamic view. Under such an assumption, the fully charged capacity of 37 C measured by the potentiostat is attributed to the production of the adduct, which can be correlated with the 6000 units of intensity measured by the microscope in channel 2. Utilizing this established calibration, we then conducted an experiment involving a charging phase under a pure nitrogen stream, followed by purging the system with a pure stream of CO_2 to capture carbon dioxide for only a short wait time afterwards. It is anticipated that the resulting intensity of the adduct, and hence the concentration, would be lower than observed in the first case (Figure 6a). Indeed, the concentration of the adduct formed under these conditions, extracted from the intensity of channel 2, is measured at 0.035 M, representing approximately 70% of the total capacity (Figure 6b). The method is equally applicable for the detection of adducts under dilute streams of CO_2. Figure 6c illustrates the data extracted from the operation of the microfluidic cell under dilute streams of 1% and 400 ppm (100% included for comparison). We

9

371 observe the formation of 0.025 M of the $BTMAPAQ(CO_2)_2^{2-}$ adduct under the dilute condition of 0.01 bar
372 CO_2 (1% CO_2, 99% N_2) within 50 minutes, detected in real-time during the formation. This short
373 timeframe (50 minutes) appears insufficient for any adduct to form under the 400 ppm condition.
374 Moreover, the method is robust enough to be employed for the extraction of kinetic rates of adduct
375 formation chemical reactions (Figure 6d). To achieve this, we increased the imaging rate to sub-second
376 intervals (125 ms) and conducted experiments using 1,5BTMAPAQ and 1,8BTMAPAQ isomers. Through
377 CV analysis, we demonstrated a kinetic rate constant for the 1,5BTMAPAQ isomer almost three times that
378 of the 1,8BTMAPAQ isomer (Table S1). The *in situ* fast imaging of the adduct formation for the two
379 isomers similarly reveals a threefold difference in kinetic rates.

380 Further incorporation of CO_2 sensors and flowmeters into the negolyte reservoir's path would enable a
381 direct comparison between the adduct concentration measured by the fluorescence microscope and the
382 total captured capacity measured by the CO_2 sensor and the flow meter. Other possibilities include
383 combining in situ fluorescence techniques with other in situ methods, such as Raman spectroscopy [28,29].
384 Moreover, establishing a rigorous correlation between intensity and concentration is crucial for enhancing
385 the reliability and accuracy of quantification processes. Additionally, as the field advances in designing
386 more stable compounds in oxygen environments, experiments can be conducted without interference from
387 oxygen over longer durations. The method provides the capability to distinguish between the oxidized,
388 reduced, and adduct species and quantify their relative concentration with sub-second time resolution
389 through their fluorescence signatures at single digit micrometer resolution, demonstrating a highly
390 promising technique for studying such systems. Furthermore, the method of conducting parallel
391 monitoring of the fluorescence signatures of the species involved in a reaction is inspiring for studying
392 reaction mechanisms and concentration quantification in other systems.

393 **Conclusions**
394 In the present work, we began by providing a thermodynamic overview of the interplay between
395 nucleophilicity-swing and pH-swing mechanisms as functions of the properties of a hypothetical quinone
396 molecule, addressing the significance of understanding the contribution of these mechanisms. We then
397 proceeded to focus on the kinetic and thermodynamic properties of the BTMAPAQ isomers as a case study,
398 revealing a strong thermodynamic tendency for BTMAPAQ to form a CO_2-adduct, though kinetically, this
399 mechanism is predicted to be slower than the pH-swing mechanism. We then proceeded to introduce two
400 techniques for the experimental differentiation between the contributions of the pH-swing mechanism and
401 nucleophilicity-swing mechanism. The first method was based on the voltage signature difference between
402 the reduced and the adduct form of the quinone, conducted by incorporating an *in situ* reference electrode.
403 In the second method, we introduced a non-invasive, *in situ* approach using fluorescence microscopy,
404 providing the unique capability to isolate the contribution of the nucleophilicity mechanism through
405 quinone-adduct quantification. This technique holds significant promise for studying similar systems in
406 detail, demonstrating a method for investigation of carbon capture processes.
407

408 **Methods**
409 *Cyclic voltammetry measurements*
410 For all three-electrode cyclic voltammetry experiments, a glassy carbon working electrode was used, accompanied
411 by an Ag/AgCl reference electrode (sourced from BASi and pre-soaked in a 3 M KCl solution), and a graphite
412 counter electrode. The electrochemical measurements, including cyclic voltammetry and linear sweep voltammetry
413 were performed using a Gamry Potentiostat.
414 *Flow cell assembly with Reference Electrode*

Flow cell experiments utilized cell hardware sourced from Fuel Cell Tech (Albuquerque, NM), and were configured into a zero-gap assembly. This setup incorporated POCO graphite flow plates, sealed with pyrolytic carbon, utilizing interdigitated flow fields for uniform distribution. Electrodes were constructed from a single layer of AvCarb HCBA carbon cloth, each with a geometric surface area of 5 cm^2. Selemion DSV-N served as the chosen anion exchange membrane. In all experiments depicted in Figure 3 utilizing the in situ reference electrode, we employed a gear pump for the negolyte, calibrated to a flow rate of 50 ml/min, and a peristaltic pump for the posolyte, optimized at 70 ml/min. The choice of a gear pump for the negolyte was based on our observations that, at these specific flow rates, the pulsation inherent to peristaltic pumps adversely affected the accuracy of the flow meter sensors. For the negolyte, a flow rate of 50 ml/min was found optimal due to the presence of the in situ reference electrode cell along its path, which has a smaller inlet diameter. A higher flow rate could potentially disturb the reference electrode setup. Consequently, the flow rates were optimized to ensure precise and stable operation. Electrochemical analysis was conducted using a Biologic SP-150e and Gamry Reference 3000 potentiostat setup. Electrolyte circulation was achieved with a Cole-Parmer Digital gear pump. Chemical reagents, including Bis((3-trimethylammonio)propyl)ferrocene dichloride (BTMAPFc) and (ferrocenylmethyl)trimethylammonium Chloride (FcNCl) from TCI-America, along with Tetramethyl ammonium chloride and tetrabutylammonium chloride from Sigma Aldrich, were employed as received, without additional purification.

For the reference electrode, a custom-made reference electrode holder was used to house an Hg/HgO reference electrode (BASi EF-1369) in the path of the electrolyte close to the inlet of the half cell. The reference electrode holder was designed with two small chambers separated by Selemion DSV-N. The chamber for the supporting electrolyte was filled with 1 M KCl, while the adjacent chamber was equipped with an inlet and outlet to allow for the flow of the battery electrolyte. Within the chamber containing the supporting electrolyte, the Hg/HgO reference electrode was submerged.

Flow cells were charged using the constant current followed by constant voltage method. Subsequently, the cells were placed in a resting state for a designated period to facilitate the completion of carbon capture. Following this, the cells were discharged, and the battery was again put into a rest mode to allow for the release of CO_2. A continuous feed gas mixture, consisting of N_2 and CO_2, was directed through the anthraquinone electrolytes, maintaining a constant flow with predetermined partial pressures. The total flow rate was 11.76 mL/min for all tests except for the tests under dilute conditions of 1% CO_2 + 99% CO_2 where the flow rate was 23.52 ml/min. FS4001 MEMS Mass Flow Sensor and SprintIR CO_2 sensor (GC-0018) were used in our tests.

Ex situ UV-vis Tests

UV-Vis absorbance spectra were obtained with a DH-2000-BAL UV-Visualization light source from Ocean Optics with optical fiber connectors, a quartz cuvette, and a cuvette holder with inlet and outlet allowing for continuous flow of electrolyte. The cuvette holder was positioned before the inlet of the flow cell. The cuvette pathlength was 100 μm. All the absorbance spectra are blank corrected.

Ex situ fluorescence plate reader

A 5 ml solution of 0.1 M 1,5-BTMAPAQ (oxidized form) was first completely reduced against 15 ml of 0.2 M BTMAPFc in a flow battery inside the glovebox. Dry ice was then transferred inside the glovebox and added to the fully reduced solution to prepare the adduct form of 1,5-BTMAPAQ. Subsequently, 200 μL of each sample (oxidized, reduced, and adduct) was loaded into separate wells of a Greiner microplate (96 well, polystyrene, flat-bottom, μclear®, black, clear bottom) inside the glovebox. To prevent reoxidation due to the diffusion of atmospheric oxygen into the electrolytes, the microplate lid was sealed before taking the samples outside of the glovebox. The microplate was then transferred outside to a BioTek Synergy HT plate reader for photophysical experiments.

Microfluidic Transparent Flow Cell

The microfluidic cell structure includes an anion exchange membrane (DSV-N) sandwiched between two 5 by 10 mm Avcarb190 porous carbon electrodes layered in pocket molded within Polydimethylsiloxane (PDMS) half cells and two acrylic end plates for compression. The half-cell has a thickness of 8 mm, suitable for direct observation with a 10x/0.3NA Leica objective (556503) with a working distance of 11 mm mounted on a confocal microscope (Leica DMi8 body with Andor dragonfly spinning disk). The unprecedented resulting transverse resolution for local

464 electrochemical characterization in porous electrode with this objective was 1 μm per pixel and about $25\mu m$ for the
465 depth of field. Peristaltic pumps were employed for circulating the electrolyte, and the headspace on the negolyte
466 side could be switched from N_2 to CO_2 during the experiments. Further information is provided in the SI.
467 *In situ fluorescence Tests*
468 Fluorescence microscopy was performed using a Leica DMi8 microscope body with a Dragonfly spinning disk
469 equipped with a Leica 10x/0.3NA HC PL FLUOTAR lens. In all imaging experiments presented in this study, the
470 following parameters were employed, unless specified otherwise: an exposure time of 2 seconds and an acquisition
471 time of 2.5 seconds per frame. Two channels were configured with an excitation wavelength of 488 and an emission
472 wavelength peaking at 594, as well as an excitation wavelength of 405 and an emission wavelength peaking at 521.
473 Further information is provided in the SI.
474 *Synthesis*
475 Synthesis of BTMAPAQs: Into a 1 L Schlenk flask, previously flame-dried, were suspended 40 mmol of
476 dihydroxyanthraquinone, 88 mmol of anhydrous K2CO3, and 9.5 mmol of KI in 160 mL of anhydrous DMF. The
477 mixture was stirred under nitrogen for 20 minutes before adding 88 mmol of 3-bromopropyl trimethylammonium
478 bromide to the resulting dark mixture. This mixture was then sealed off from the air to exclude moisture and
479 vigorously stirred at 100 °C for 16 hours, leading to a brownish slurry. Once cooled, 150 mL of ethyl acetate was
480 mixed into the slurry, stirred at room temperature for 30 minutes, and then filtered to separate the brown solid. This
481 washing step was repeated several times until the filtrate turned colorless. The solid was then dissolved in methanol,
482 and this solution was filtered to eliminate insoluble inorganic salts. Subsequently, the filtrate was evaporated under
483 reduced pressure to remove methanol, yielding a dark red solid. This solid was then dissolved in deionized water
484 and passed through a pre-prepared anion-exchange resin column to exchange bromide ions with chloride ions. The
485 resulting dark red to bright yellow (depending on concentration) solution was evaporated under reduced pressure to
486 eliminate water and retrieve the red solid. This solid was redissolved in methanol, and the saturated solution was
487 gradually added to 200 mL of ethyl acetate to precipitate out the product. The resulting precipitates were filtered to
488 obtain the final product as orange to yellow solids, with yields ranging from 85% to 95%.
489 Synthesis of 22PEAQ: Into a 100 mL pear-shaped flask, 5 grams of 2-hydroxyanthraquinone (22.3 mmol) was
490 introduced along with ethyl 2-bromopropionate (3.75 mL, 29 mmol, 1.3 equivalents) and 7.5 g of potassium
491 carbonate (54 mmol, 2.4 equivalents). The mixture was stirred in 40 mL of DMF at 80°C for 3 hours, followed by
492 vacuum filtration to isolate the ester. The ester, without undergoing further purification, was then dispersed in a
493 mixture of 30 mL water and 30 mL isopropanol, to which 7.5 g of potassium hydroxide (133 mmol, 16 equivalents)
494 was added. This mixture was stirred at 80°C for another 3 hours and then precipitated using 1 M HCl to obtain a
495 green solid. The process yielded 2.4 g of the product, representing a 52.9% yield.
496 Synthesis of D2PEAQ: Ten grams of 2,6-dihydroxyanthraquinone (41.6 mmol) were combined with 15 grams of
497 potassium carbonate (108 mmol, 2.6 equivalents), 15 mL of methyl 2-bromopropionate (22.45 g, 134.4 mmol, 3.23
498 equivalents), and 30 mL of dimethylformamide. The mixture was stirred at 80°C for one hour, leading to the
499 formation of three sandy yellow precipitates. Subsequently, 20 mL of water was introduced to rinse the flask,
500 followed by vacuum filtration. The resulting solid, without undergoing any purification, was then dispersed in a
501 mixture of 150 mL of 2-propanol and 150 mL of water, with the addition of 15 grams of potassium hydroxide (267
502 mmol, 6.43 equivalents). This mixture was agitated at 80°C for three hours, after which 1.5 M hydrochloric acid
503 was added gradually until a yellow precipitate formed. The final mixture was vacuum filtered to obtain a yellow
504 solid, with a final yield of 9.15 grams (57%).
505
506 **Data Availability**
507 Further data supporting the findings of this study is provided in the Supplementary Information section.
508 All the source data for this article (both the main manuscript and the SI) is openly available at xx.
509
510 **Code Availability**
511 The code written for solving the set of equilibrium equations described in the Thermodynamic Overview
512 section is available at xx.

Author Contributions

M.J.A. and R.G.G. supervised the project. K.A. and M.J.A. conceived the idea. K.A. developed the thermodynamic model with input from Y.J. and D.X.; M.S.E. implemented the code, and K.A. analyzed the data. Y.J. synthesized BTMAPAQ isomers. E.F.K. synthesized 22PEAQ and D2PEAQ compounds. K.A. conducted the CV tests on the BTMAPAQ isomers. J.D.S. developed and implemented the model for CV fittings. K.A. conducted *in situ* tests with the reference electrode and analyzed the data. K.A. and M.A. performed *ex situ* UV-Vis tests and analyzed the data. K.A. carried out *ex situ* fluorescence plate reader tests. T.C. designed and built the transparent microfluidic flow cell. K.A. and T.C. performed the *in situ* fluorescence tests and analyzed the data. All authors contributed to the discussion. K.A. wrote the manuscript, with all co-authors contributing to the editing.

Declaration of Interests

The authors declare no competing interests.

Figure Captions

Figure 1 Equilibrium concentrations derived from solving equilibrium equations. Unless specified, a total concentration of 0.1 M AQ dissolved under a partial pressure of 0.1 bar is assumed. The AQ pK_{a1} and pK_{a2} values are set at 11 and 13, respectively, with equilibrium constants K_4, K_5, and K_w at $1.1 * 10^{-6}$ M, $4.1 * 10^{-10}$ M, and 10^{-14} M^2, respectively, and K_{AQ_adduct} of 10^{14} M^{-2}. a) Concentration profiles of HCO_3^-, CO_3^{2-}, $CO_2(aq)$, $AQ(CO_2)_2^{2-}$ at different K_{AQ_adduct} values. b) Concentrations of HCO_3^-, CO_3^{2-}, $CO_2(aq)$, $AQ(CO_2)_2^{2-}$ at varying pK_{a2} values of the AQ molecule. c) Concentrations of HCO_3^-, CO_3^{2-}, $CO_2(aq)$, $AQ(CO_2)_2^{2-}$ at different partial pressures of CO_2. d) Concentrations of AQ^{2-}, $AQ(CO_2)_2^{2-}$, AQ, AQH^- at different partial pressures of CO_2.

Figure 2 Molecular structures and cyclic voltammetry profiles of BTMAPAQ isomers. 5 mM of a) 1,4-BTMAPAQ, b) 1,5-BTMAPAQ and c) 1,8-BTMAPAQ dissolved in 1 M KCl under a pure CO_2 headspace at different scan rates between 100 mV/s to 1000 mV/s. For comparison, the cyclic voltammetry profile under a pure N_2 headspace is also depicted as a dashed line at a scan rate of 300 mV/s for each isomer. d) The experimental and fitted cyclic voltammetry profiles of 1,8-BTMAPAQ for three scan rates of 0.1 V/s, 0.5 V/s, and 0.9V/s.

Figure 3 Flow cell operation of 1,5-BTMAPAQ with in situ reference electrode. a) Upstream gas ratio, voltage, pH, measured partial pressure of CO_2, and flow rate at the downstream measured during the experiment utilizing a flow cell comprising 12 ml of 0.1 M 1,5BTMAPAQ paired with 40 ml of 0.2 M BTMAPFc. The cell was charged in a nitrogen environment, followed by a controlled purge with 0.1 bar CO_2 and 0.9 bar N_2 for 60 minutes followed by a switch back to the nitrogen environment. b) (Top) Zoomed in full-cell voltage of the battery shown in Figure 3a, and (bottom) negative half-cell potential measured via *in situ* reference electrode during operation. c) Full-cell

558 and negative half-cell potentials of the cell operated under different duration of CO_2 purge time. The solid lines
559 depict experiments where the charge itself was conducted under N_2, whereas for the dashed line experiments, the
560 purging with CO_2 is conducted from the beginning of the charge phase. d) (Top) CO_2 release volume calculated
561 from the CO_2 sensor measurements and the oxidation voltage signature of the adduct. For comparison, the maximum
562 theoretical CO_2 release volume calculated from the total discharge capacity is also shown. (Bottom) the percentage
563 contribution of each mechanism to the total capture amount. e) CO_2 release volume calculated from the CO_2 sensor
564 measurements and the oxidation voltage signature of the adduct for 7 ml of 0.4 M of 1,4-BTMAPAQ and very
565 diluted CO_2 concentrations of 0.01 bar (1% CO2, 99% N_2) under different rest durations. Note that the CO_2 sensor
566 has an accuracy of ± 300 ppm $\pm 5\%$ of the reading, and the flow meter has an accuracy of $\pm 1.5\%$ (0-30 sccm) based
567 on their specifications (see SI Section 5.4).

568 **Figure 4 Absorbance and emission spectra of 1,5-BTMAPAQ under different experimental conditions.** a) *In*
569 *Situ* absorbance spectra of 5 mM 1,5-BTMAPAQ dissolved in 1 M KCl during the charging phase (reduction of
570 BTMAPAQ) in a battery operating versus 40 mM BTMAPFc in 1 M KCl under pure nitrogen phase. The absorbance
571 spectra were taken until the charge was complete. b) *In Situ* absorbance spectra of 5 mM 1,5-BTMAPAQ dissolved
572 in 1 M KCl taken during the rest time immediately after the charging phase. In the first minute, 50% CO_2/50% N_2
573 was introduced to the solution. c) *Ex situ* fluorescence spectra of 100 mM of the adduct, reduced and oxidized
574 species of 1,5-BTMAPAQ excited at 405 nm. d) *Ex-situ* fluorescence spectra of 100 mM of the adduct, reduced and
575 oxidized species of 1,5-BTMAPAQ excited at 475 nm.

576 **Figure 5 In situ electrochemical fluorescence microscopy for carbon capture: setup and operation**. a)
577 Schematic of the custom-designed optically transparent microfluidic inspired flow cell designed for the in situ
578 electrochemical investigation. b) Widefield optical microscopy image of the porous carbon paper electrode inside
579 the electrochemical cell. c) Experimental setup for the study of the electrochemical carbon capture flow cells using
580 in situ fluorescence microscopy. d) Capacity, average over an entire image normalized intensity (normalized based
581 on the initial intensity), and pH during the operation of the microfluidic cell containing 4 ml of 0.1 M 1,5 BTMAPAQ
582 in 1 M KCl paired with 20 ml of 0.2 M BTMAPFc in 1 M KCl under the fluorescence microscope. e) Normalized
583 intensity at a pixel level (1 μm) of the two channels at times of interest (t_0, t_1, t_2, and t_3) shown with arrows in Figure
584 5d (in the normalized intensity subplot).

585 **Figure 6 Information extracted from the operation of the microfluidic flow cell under the fluorescence**
586 **microscope**. The flow cell was operated under nitrogen and carbon dioxide streams, monitoring channels with
587 excitation and absorption wavelengths of 488/594, respectively in channel 1 and 405/521, respectively for channel
588 2. Channel 1 wavelengths correspond to the reduced form concentration and channel 2 correspond to the adduct
589 concentration. a) Voltage, capacity, in situ fluorescence intensity and pH of a solution of 5 mM 1,5-BTMAPAQ
590 dissolved in 1 M KCl under pure stream of CO_2. b) Voltage, capacity, concentration (extracted from in situ
591 fluorescence intensity) and pH of a solution of 5 mM 1,5-BTMAPAQ dissolved in 1 M KCl under pure stream of
592 CO_2. c) Capacity, adduct concentration and pH at three different CO_2 partial pressures mixed with nitrogen. d)
593 Normalized intensity of adduct versus time measured with increased imaging rate to sub-second intervals (125 ms)
594 for two isomers of 1,5BTMAPAQ and 1,8BTMAPAQ.

595
596

References

598 [1]M. Bui, C.S. Adjiman, A. Bardow, E.J. Anthony, A. Boston, S. Brown, P.S. Fennell, S. Fuss, A. Galindo, L.A. Hackett,
599 J.P. Hallett, H.J. Herzog, G. Jackson, J. Kemper, S. Krevor, G.C. Maitland, M. Matuszewski, I.S. Metcalfe, C.
600 Petit, G. Puxty, J. Reimer, D.M. Reiner, E.S. Rubin, S.A. Scott, N. Shah, B. Smit, J.P.M. Trusler, P. Webley, J.
601 Wilcox, and N. Mac Dowell, "Carbon Capture and Storage (Ccs): The Way Forward", *Energy &*
602 *Environmental Science* **11**, 1062 (2018). https://doi.org/10.1039/c7ee02342a
603 [2]G.T. Rochelle, "Amine Scrubbing for CO2 Capture", *Science* **325**, (2009).

604 [3] G.T. Rochelle, "Thermal Degradation of Amines for CO2 Capture", *Current Opinion in Chemical Engineering* **1**, 183
605 (2012). https://doi.org/10.1016/j.coche.2012.02.004
606 [4] K.M. Diederichsen, R. Sharifian, J.S. Kang, Y. Liu, S. Kim, B.M. Gallant, D. Vermaas, and T.A. Hatton, "Electrochemical
607 Methods for Carbon Dioxide Separations", *Nature Reviews Methods Primers* **2**, (2022).
608 https://doi.org/10.1038/s43586-022-00148-0
609 [5] J.H. Rheinhardt, P. Singh, P. Tarakeshwar, and D.A. Buttry, "Electrochemical Capture and Release of Carbon
610 Dioxide", *ACS Energy Letters* **2**, 454 (2017). https://doi.org/10.1021/acsenergylett.6b00608
611 [6] M. Rahimi, A. Khurram, T.A. Hatton, and B. Gallant, "Electrochemical Carbon Capture Processes for Mitigation of
612 Co(2) Emissions", *Chem Soc Rev* **51**, 8676 (2022). https://doi.org/10.1039/d2cs00443g
613 [7] Y. Liu, H.Z. Ye, K.M. Diederichsen, T. Van Voorhis, and T.A. Hatton, "Electrochemically Mediated Carbon Dioxide
614 Separation with Quinone Chemistry in Salt-Concentrated Aqueous Media", *Nat Commun* **11**, 2278 (2020).
615 https://doi.org/10.1038/s41467-020-16150-7
616 [8] X. Li, X. Zhao, Y. Liu, T.A. Hatton, and Y. Liu, "Redox-Tunable Lewis Bases for Electrochemical Carbon Dioxide
617 Capture", *Nature Energy* **7**, 1065 (2022). https://doi.org/10.1038/s41560-022-01137-z
618 [9] S. Jin, M. Wu, R.G. Gordon, M.J. Aziz, and D.G. Kwabi, "pH Swing Cycle for CO_2 Capture Electrochemically Driven
619 through Proton-Coupled Electron Transfer", *Energy & Environmental Science* **13**, 3706 (2020).
620 https://doi.org/10.1039/d0ee01834a
621 [10] S. Jin, M. Wu, Y. Jing, R.G. Gordon, and M.J. Aziz, "Low Energy Carbon Capture via Electrochemically Induced pH
622 Swing with Electrochemical Rebalancing", *Nature communications* **13**, 1 (2022).
623 https://doi.org/https://doi.org/10.1038/s41467-022-29791
624 [11] B. Gurkan, F. Simeon, and T.A. Hatton, "Quinone Reduction in Ionic Liquids for Electrochemical CO2 Separation",
625 *ACS Sustainable Chemistry & Engineering* **3**, 1394 (2015).
626 https://doi.org/10.1021/acssuschemeng.5b00116
627 [12] K.M. Diederichsen, Y. Liu, N. Ozbek, H. Seo, and T.A. Hatton, "Toward Solvent-Free Continuous-Flow
628 Electrochemically Mediated Carbon Capture with High-Concentration Liquid Quinone Chemistry", *Joule* **6**,
629 221 (2022). https://doi.org/10.1016/j.joule.2021.12.001
630 [13] J.M. Barlow and J.Y. Yang, "Oxygen-Stable Electrochemical Co(2) Capture and Concentration with Quinones Using
631 Alcohol Additives", *J Am Chem Soc* **144**, 14161 (2022). https://doi.org/10.1021/jacs.2c04044
632 [14] S. Voskian and T.A. Hatton, "Faradaic Electro-Swing Reactive Adsorption for CO_2 Capture", *Energy & Environmental
633 Science* **12**, 3530 (2019). https://doi.org/10.1039/c9ee02412c
634 [15] D. Wielend, D.H. Apaydin, and N.S. Sariciftci, "Anthraquinone Thin-Film Electrodes for Reversible CO2 Capture
635 and Release", *Journal of Materials Chemistry A* **6**, 15095 (2018). https://doi.org/10.1039/c8ta04817g
636 [16] Y. Jing, K. Amini, D. Xi, S. Jin, A. Alfaraidi, E. Kerr, R. Gordon, and M. Aziz, "Electrochemically Induced CO2 Capture
637 Enabled by Aqueous Quinone Flow Chemistry", *ChemRxiv* (2023). https://doi.org/10.26434/chemrxiv-
638 2023-nfg6z
639 [17] C.L. Chuanliang Huang, Kejing Wu, Hairong Yue, Siyang Tang, Houfang Lu, Bin Liang, "CO2 Capture from Flue Gas
640 Using an Electrochemically Reversible Hydroquinone/Quinone Solution", *Energy & Fuels* **33**, 3380 (2019).
641 https://doi.org/10.1021/acs.energyfuels.8b04419
642 [18] L. Luo, L. Hou, Y. Liu, K. Wu, Y. Zhu, H. Lu, and B. Liang, "Regeneration of Na2q in an Electrochemical CO2 Capture
643 System", *Energy & Fuels* **35**, 12260 (2021). https://doi.org/10.1021/acs.energyfuels.1c00960
644 [19] E.F. Kerr, Z. Tang, T.Y. George, S. Jin, E.M. Fell, K. Amini, Y. Jing, M. Wu, R.G. Gordon, and M.J. Aziz, "High Energy
645 Density Aqueous Flow Battery Utilizing Extremely Stable, Branching-Induced High-Solubility
646 Anthraquinone near Neutral pH", *ACS Energy Letters* **8**, 600 (2022).
647 https://doi.org/10.1021/acsenergylett.2c01691
648 [20] D.G. Kwabi, Y. Ji, and M.J. Aziz, "Electrolyte Lifetime in Aqueous Organic Redox Flow Batteries: A Critical Review",
649 *Chem Rev* **120**, 6467 (2020). https://doi.org/10.1021/acs.chemrev.9b00599
650 [21] M. Wu, M. Bahari, Y. Jing, K. Amini, E.M. Fell, T.Y. George, R.G. Gordon, and M.J. Aziz, "Highly Stable, Low Redox
651 Potential Quinone for Aqueous Flow Batteries", *Batteries & Supercaps* e202200009 (2022).
652 https://doi.org/https://doi.org/10.26434/chemrxiv-2021-rjzdn).

653   [22]L.N.R. Rabindra N. Roy, Kathleen M. Vogel, C. Porter-Moore, Tara Pearson, and F.J.M. Catherine E. Good, Douglas
654   M. Campbell "The Dissociation Constants of Carbonic Acid in Seawater at Salinities

655   5 to 45 and Temperatures 0 to 45°C", *Marine Chemistry* **44**, 249 (1993).

656   [23]F. Simeon, M.C. Stern, K.M. Diederichsen, Y. Liu, H.J. Herzog, and T.A. Hatton, "Electrochemical and Molecular
657   Assessment of Quinones as CO2-Binding Redox Molecules for Carbon Capture", *The Journal of Physical*
658   *Chemistry C* **126**, 1389 (2022). https://doi.org/10.1021/acs.jpcc.1c09415

659   [24]W.C. Xiaoguang Wang, Robert Burns, Nichola McCann, and Marcel Maeder, "Comprehensive Study of the
660   Hydration and Dehydration Reactions of Carbon Dioxide Inaqueous Solution", *Journal of Physical Chemistry*
661   *A* **114**, 1734 (2009).

662   [25]E.W. Zhao, T. Liu, E. Jonsson, J. Lee, I. Temprano, R.B. Jethwa, A. Wang, H. Smith, J. Carretero-Gonzalez, Q. Song,
663   and C.P. Grey, "In Situ NMR Metrology Reveals Reaction Mechanisms in Redox Flow Batteries", *Nature* **579**,
664   224 (2020). https://doi.org/10.1038/s41586-020-2081-7

665   [26]K. Amini, Y. Jing, J. Gao, J.D. Sosa, R.G. Gordon, and M.J. Aziz, "Electrochemical Performance of Mixed Redox-
666   Active Organic Molecules in Redox Flow Batteries", *Journal of The Electrochemical Society* (2023).
667   https://doi.org/10.1149/1945-7111/ad1295

668   [27]K. Amini, E.F. Kerr, T.Y. George, A.M. Alfaraidi, Y. Jing, T. Tsukamoto, R.G. Gordon, and M.J. Aziz, "An Extremely
669   Stable, Highly Soluble Monosubstituted Anthraquinone for Aqueous Redox Flow Batteries", *Advanced*
670   *Functional Materials* (2023). https://doi.org/10.1002/adfm.202211338

671   [28]X. Lu, C. Zhu, Z. Wu, J. Xuan, J.S. Francisco, and H. Wang, "In Situ Observation of the pH Gradient near the Gas
672   Diffusion Electrode of Co(2) Reduction in Alkaline Electrolyte", *J Am Chem Soc* **142**, 15438 (2020).
673   https://doi.org/10.1021/jacs.0c06779

674   [29]K.J. Lamb, M.R. Dowsett, K. Chatzipanagis, Z.W. Scullion, R. Kroger, J.D. Lee, P.M. Aguiar, M. North, and A. Parkin,
675   "Capacitance-Assisted Sustainable Electrochemical Carbon Dioxide Mineralisation", *ChemSusChem* **11**, 137
676   (2018). https://doi.org/10.1002/cssc.201702087

677

678

679
680